ADVANCED MATERIALS
www.advmat.de

# Spatiotemporal Evolution in Hard Carbon Synthesis via Electrothermal Coupling Strategy for High-Performance Sodium-Ion Batteries

*Pengfei Huang, Zhaoxin Guo, Zekun Li, Li Chen, Wei-Di Liu, Jiawei Luo, Zhedong Liu, Jingchao Zhang, Jianrong Zeng, Wenjun Zhang, Xinxi Zhang, Rongtao Zhu,* and Yanan Chen**

**Conventional hard carbon synthesis through prolonged sintering suffers from structural degradation, including amorphous-to-graphitic transitions and pore collapse, critically impairing sodium storage performance. Here, a spatiotemporally controlled electrothermal coupling strategy is proposed that revolutionizes carbonization via in situ joule heating, achieving ultrafast synthesis (30 s) with preserved structural integrity. By precisely regulating current density distribution, this method enables defect-selective graphitization while maintaining abundant micropores and expanded interlayer spacing (0.39 nm). The optimized hard carbon synthesized at 1000 °C demonstrates exceptional sodium storage capacity (306.83 mAh $g^{-1}$) and record-high initial Coulombic efficiency (91.99%), outperforming furnace sample by 16.7% in capacity. During the spatiotemporal evolution process, localized electric field can induce directional charge redistribution and lower C—C bond dissociation barriers, enabling rapid formation of microporous structure with enhanced $Na^+$ diffusion kinetics and stable interfacial properties. Temporal superiority of this method is evidenced by 79.45% capacity retention after 1000 cycles. This work establishes a paradigm for energy-efficient carbon material synthesis via spatiotemporal electrothermal control, providing fundamental insights into field-assisted reaction kinetics for next-generation battery manufacturing.**

## 1. Introduction

Hard carbon materials, due to their unique structural characteristics and excellent electrochemical performance, have emerged as ideal anode materials for commercial sodium-ion batteries (SIBs).[1] Compared to traditional lithium-ion batteries, SIBs offer extensive advantages in terms of earth abundance, cost, and environment impact, making them a key component of next-generation sustainable energy storage systems.[2] However, conventional production of hard carbon materials relies on energy-intensive tube furnaces (with a heating rate of 10–20 °C $min^{-1}$ and a dwell time of 2–10 h at temperature ranging from 1000 to 1600 °C), which increases energy consumption, refrains production efficiency and hinders improvement of material performance.[3]

In the conventional production methods of hard carbon materials, heat is transferred through conduction and convection, which can create temperature

P. Huang, Z. Guo, Z. Li, L. Chen, J. Luo, Z. Liu, J. Zhang, Y. Chen
School of Materials Science and Engineering
Key Laboratory of Advanced Ceramics
Machining Technology of Ministry of Education
Tianjin Key Laboratory of Composite and Functional Materials
Tianjin University
Tianjin 300072, P. R. China
E-mail: yananchen@tju.edu.cn

P. Huang, W. Zhang, X. Zhang, R. Zhu
School of Chemical Engineering and Technology
China University of Mining and Technology
Xuzhou, Jiangsu 221116, P. R. China
E-mail: rtzhu2010@cumt.edu.cn

W.-D. Liu
School of Chemistry and Physics
ARC Research Hub in Zero-emission Power Generation for Carbon Neutrality, and Centre for Materials Science
Queensland University of Technology
Brisbane, QLD 4000, Australia

J. Zeng
Shanghai Synchrotron Radiation Facility
Shanghai Advanced Research Institute
Chinese Academy of Sciences
Shanghai 201204, P. R. China

J. Zeng
Shanghai Institute of Applied Physics
Chinese Academy of Sciences
Shanghai 201800, P. R. China

The ORCID identification number(s) for the author(s) of this article can be found under https://doi.org/10.1002/adma.202507521

DOI: 10.1002/adma.202507521

 

gradients within the material.[4] Such uneven temperature distribution during the carbonization process can lead to non-uniform reactions, resulting in an inhomogeneous structural and morphological features in as-produced hard carbon material.[5] These inhomogeneity can cause fluctuations in electrochemical performance, particularly the sodium storage capacity, potentially manifested as poor cycling stability and lower specific capacity.[6] Furthermore, conventional production methods typically require long heat treatment durations to complete the carbonization process, which will inevitably slow down the structural and morphological evolution.[7] This gradual evolution can lead to the graphitization or excessive carbonization of amorphous carbon within the hard carbon material, reducing its amorphous level.[8] The amorphous content in hard carbon plays a vital role in determining its sodium storage performance, as amorphous carbon offers more sodium storage sites and broader ion diffusion channels compared to its more ordered counterparts.[9] Therefore, excessive heat treatment inevitably leads to reduced amount of sodium storage sites, and deteriorates both the capacity and rate performance.[10]

Joule heating technique has demonstrated unique advantages in the field of nanomaterial synthesis in recent years.[11–13] This technique applies a high-density current to conductive precursors, utilizing intrinsic resistance of the precursors to achieve instantaneous bulk heating, with heating rates of $10^3$–$10^4$ °C $s^{-1}$).[14] This heating rate entirely bypasses conventional heat conduction paths.[15] The core mechanism underlying this technology is the coupling effects of electric, thermal, and mechanical forces. Under an applied electric field, charge carriers (electrons and ions) accelerated by the field collide with the crystal lattice, generating heat through the Joule heating process and leading to rapid temperature rises.[16] In addition, electromigration-driven by momentum transfer from the electron wind -promotes grain boundary migration, and Lorentz forces acting on current-carrying regions introduce magneto-mechanical stresses that drive dislocation motion and broader microstructural rearrangements.[17] Theoretical studies indicate that these coupling effects can lead to topological reconstruction of materials in the subsecond timescale, with energy conversion efficiency improved by 2–3 orders of magnitude compared to traditional heating methods.[18] However, traditional sintering and pyrolysis techniques lack the spatial and temporal precision to exploit these effects, often leading to uncontrolled graphitization, loss of microporosity, and insufficient interlayer expansion.

In this study, we address the inherent limitations of conventional sintering in hard carbon synthesis by proposing a spatiotemporally controlled electrothermal coupling strategy. By integrating precise regulation of current density with ultrafast Joule heating (100 °C $s^{-1}$), we achieve dynamic control over structural evolution, enabling defect-selective graphitization while preserving critical microporous architectures and expanded interlayer spacing. Our approach suppresses structural degradation mechanisms—such as amorphous-to-graphitic phase collapse and pore closure. Multi-scale simulations coupled with operando characterization elucidate how localized electric fields lower energy barriers for carbon precursor reorganization, simultaneously accelerating microcrystal growth and stabilizing ionic diffusion pathways. This work bridges the critical gap between rapid synthesis kinetics and structural precision in carbon materials, offering a universal framework for designing high-performance sodium-ion battery anodes through spatiotemporal electrothermal engineering.

## 2. Results and Discussion

### 2.1. Thermodynamic Analysis of Ultrafast Joule Heating Process

Traditional heating methods, as schematically shown in **Figure 1a**, relies on heat conduction or convection, such as heating via tube or muffle furnaces requiring prolonged heating (Figure 1b) of >2 h. However, long-time dwelling at high temperature can induce graphitization or over-carbonization of the amorphous carbon within hard carbon materials. In contrast, Figure 1c shows the temperature profile for Joule heating using a home-made carbonization device (Figure S1, Supporting Information),[19] which relies on its own resistance for in situ heating.[20] This method allows rapid heating (100K $s^{-1}$) and cooling (50 K $s^{-1}$) without generating temperature gradients, enabling rapid heating of the sample. As shown in Figure S2 (Supporting Information), when the Joule heating device is operating, the sample emits a uniform yellow light, indicating that the temperature distribution across the entire sample is homogeneous, which is crucial for precise control of the carbonization process.

To compare the difference between various heating methods, COMSOL Multiphysics software was employed for heat transfer dynamics simulation and temperature distribution analysis. A 2D model was constructed for traditional heating methods (using a tubular furnace as an example) (Figure S3; Table S1, Supporting Information). Figure S4 (Supporting Information) illustrates the temperature distribution characteristics at different heating rates. When heated to 1000 °C within 20 min (Figure S5, Supporting Information), the maximum temperature difference within the sample could reach up to 800 °C, indicating that rapid heating via traditional heating methods can result in a significant temperature gradient. This inhomogeneous temperature distribution requires traditional heating methods to extend the processing time (usually several hours). In contrast, the simulation results of Joule heating (Figure S6, Supporting Information) show that within a short heating time (10 s), the sample exhibits a more uniform temperature distribution (Figure 1c,d). This inherent uniformity at the laboratory scale, as supported by our COMSOL simulations, is a significant advantage. When considering scalability, the principle of in situ heating remains advantageous. The direct generation of heat within the material provides a fundamental basis for achieving better temperature control; even at larger scales, this is expected to lead to more uniform heating effects and higher energy efficiency compared to indirect heating methods.

Combing analysis of synchrotron radiation-based pair distribution function (PDF) analysis of the atomic spacing distribution in carbon materials (Figure 1e), the temperature-time plot recorded in Figure 1c, and the PDF peak evolution in Figure S7 (Supporting Information), the local structural evolution and phase transition kinetics during Joule heating can be comprehensively revealed. The Joule heating process consists of three stages: a 10-s heating period, a 30-s dwelling period, and a 20-s cooling period. Quantitative analysis in Figure 1f shows that the first

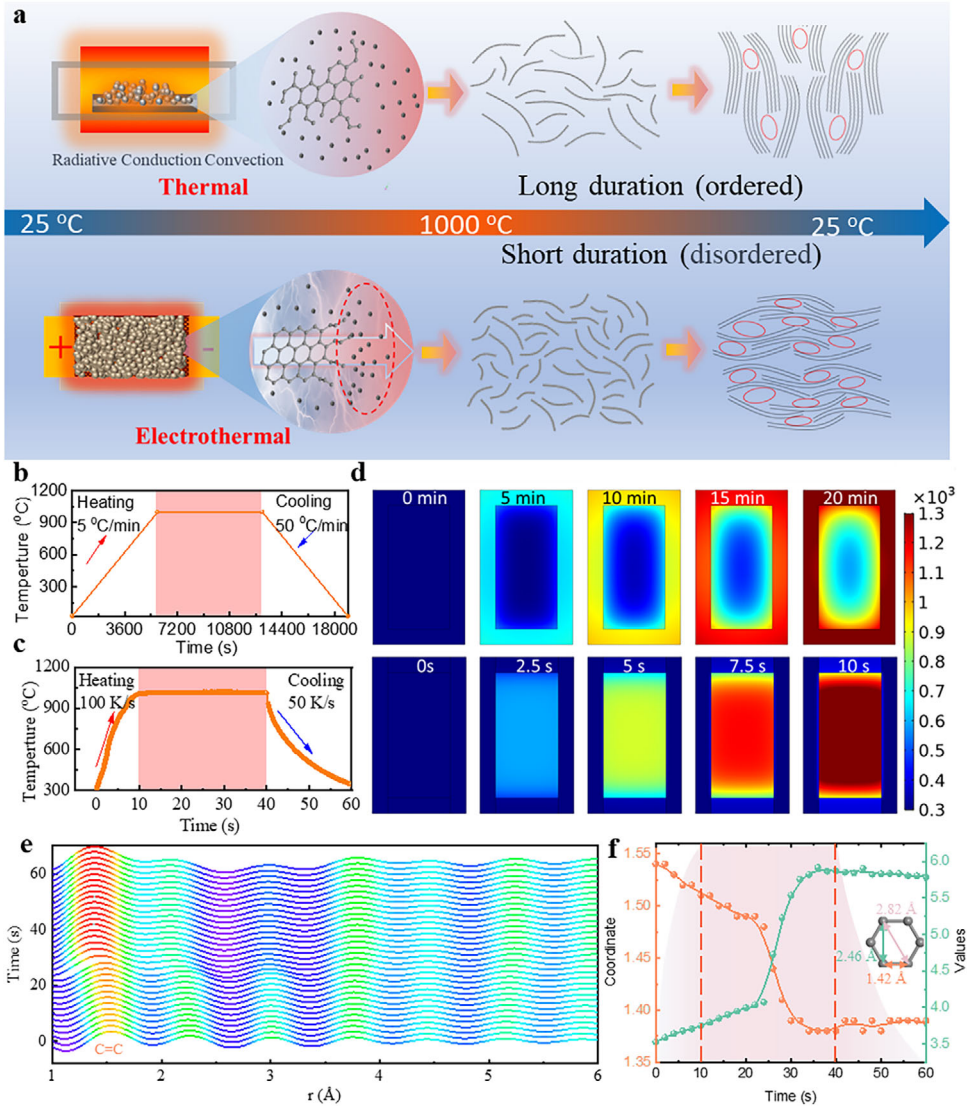


**Figure 1.** Thermodynamic analysis of the tube furnace and Joule-heated samples: a) Schematic diagram of carbon microcrystalline changes in the tube furnace and Joule-heated samples; b) Temperature-time curve for tube furnace heating; c) Temperature-time curve for Joule-heated samples; d) Finite element simulation of heat transfer process for the tube furnace (0–20 min) and Joule-heated samples (0–10 s); e) In situ synchrotron radiation PDF profiles during ultrafast Joule heating; f) Evolution of the first peak intensity and position (nearest-neighbor C═C atomic distance) in the PDF over time.

characteristic peak (C═C nearest-neighbor distance) undergoes significant displacement during the 30-s dwelling period, where the radial distribution function G(r) intensity increases from 3.5 to 6.0 corresponding to a 71% increase in coordination number. The peak position shifts from 1.54 Å to a lower r value by 0.15 Å, with the atomic spacing contraction rate of 9.7%. All measured parameters stabilize within 30 s of thermal activation, indicating that Joule heating drives the amorphous-to-graphite microcrystal transformation to completion in this timeframe.

### 2.2. Spatiotemporal Evolution Process

To further elucidate the temperature-induced structural evolution process of carbon materials (**Figure 2**), Raman spectroscopy analysis was conducted (Figure 2a–c). The results show that as the treatment temperature increases from 900 to 1300 °C, the intensity ratio between the disorder peak (D peak, 1350 $cm^{-1}$) and the graphitization peak (G peak, 1580 $cm^{-1}$) ($I_D/I_G$) decreases from 1.395 to 0.702. This indicates a significant improved the $sp^2$ hybridization level (Table S2, Supporting Information). This finding correlates with the XRD patterns (Figure 2d–f), where the (002) diffraction peak shifts to higher angles with increasing heat treatment temperature, indicating the shrinkage of interlayer spacing ($d_{nn2}$) from 0.383 nm to 0.358 nm. At higher heat treatment temperature, both the vertical (Lc) and lateral (La) crystallite sizes significantly increase, reflecting enhanced crystallinity.

High-Resolution Transmission Electron Microscopy (HRTEM) images of hard carbon samples heated from 900

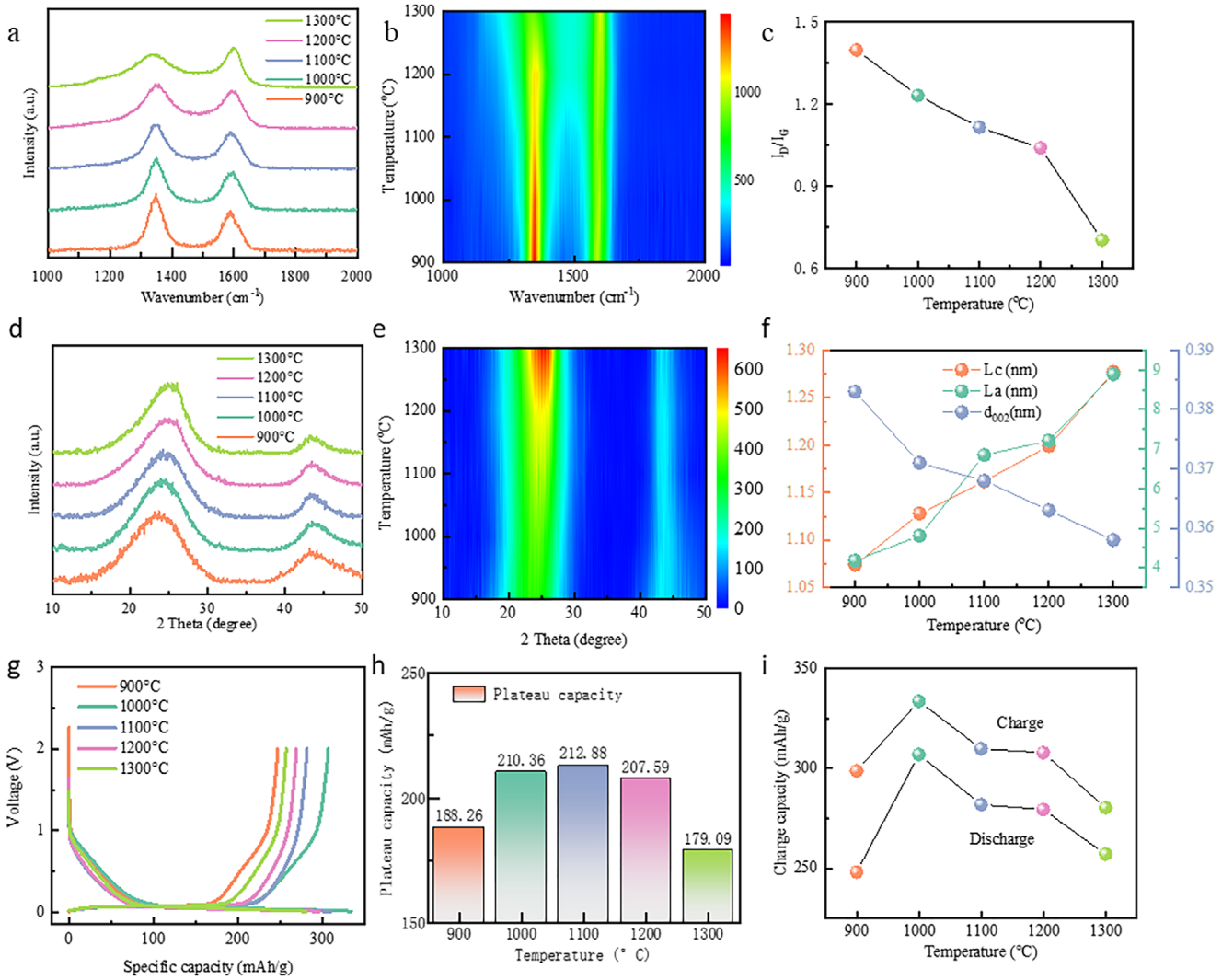


**Figure 2.** Structural evolution and electrochemical assessment of Joule-heated hard carbon: a,b) Raman spectra at different temperatures; c) Evolution of the $I_D/I_G$ peak ratio with temperature; d,e) XRD patterns at different temperatures; f) Evolution of Lc, La, and $d_{002}$ with temperature; g) Charge-discharge profiles of sodium-ion batteries using hard carbon prepared at different temperatures; h) Plateau capacity (below 0.1 V) in the charge curves of hard carbon at different temperatures; i) Charge-discharge capacity at different temperatures.

to 1300 °C (Figure S8, Supporting Information) further validate the observed temperature-dependent structural ordering. Detailed analysis of these images and the extracted carbon microcrystal structures (Figures S9–S13, Supporting Information) shows that ordering intensifies as temperature increases. Correspondingly, as illustrated in Figure S14 (Supporting Information) (panels a1–a5), the average microcrystal length grows from 0.62 to 0.67 nm over this temperature range. This suggests that high heat treatment temperature can boost atom movement and promote the dissolution of smaller microcrystals into larger ones. In parallel, a decrease in carbon layer curvature (leftward shift in the distribution curves, Figure S14$b_{1\text{-}5}$, Supporting Information) indicates that high temperature can straighten bent carbon chains, and facilitate the planarization of the $sp^2$ hybridized network. The evolution of carbon layer orientation (leftward shift of curves in Figure S14$c_{1\text{-}5}$, Supporting Information) shows that van der Waals and $\pi$-$\pi$ interactions dominate at the heat treatment temperature of >1000 °C, driving the formation of preferential orientations and the transition from short-range to long-range ordering. The continuous shrinkage of the interlayer spacing ($d_{nn2}$) (Figure S14$d_{1\text{-}5}$, Supporting Information) results from enhanced interlayer conjugation and increased $sp^2$ hybridization level. Additionally, PDF analysis of samples after heat treatment at various temperatures (Figure S15, Supporting Information) reveals that the intensity of the first characteristic peak increases with rising treatment temperature, indicating an increase in atomic coordination number. The lattice parameter analyses illustrate the thermally driven crystallization mechanism of the carbon network. SEM analysis (Figure S16a–e, Supporting Information) quantitatively shows that the particle size increases from 2–4 µm (900 °C) to 5–6 µm (1300 °C) with increasing heat treatment temperature from 900 to 1300 °C. At the same time, the surface morphology gradually evolves from rough to smooth: a smoother surface is shown

at high temperature, corresponding to the enhanced degree of graphitization; while the rough structure retained at low temperature reflects the limited graphitization.

Figure 2g–i compares the electrochemical performance of Joule heating temperature ranging from 900 to 1300 °C. The low-voltage plateau capacity (below 0.1 V) is widely understood to primarily reflects sodium storage in micropores of hard carbon, particularly benefiting from the presence and extent of closed pore structures. Conversely, the sloping capacity (above 0.1 V) is generally attributed to sodium adsorption on surfaces and defects, or intercalation into less ordered graphitic regions.[21] At a synthesis temperature of 900 °C, the material exhibits a relatively low plateau capacity. This suggests that at this temperature, the thermal energy may be insufficient for the extensive carbon rearrangement and graphitization typically required for the optimal development of closed pores. Upon increasing the Joule heating temperature to 1000 °C, a significant enhancement in the plateau capacity increases is observed, reaching 210.36 mAh $g^{-1}$. This increase strongly suggests that 1000 °C provides more favorable conditions for the formation and evolution of a well-defined microporous structure, likely including a greater volume of the crucial closed pores. At this temperature, the charge-discharge capacity reaching its peak values (306.83 and 333.55 mAh $g^{-1}$), resulting in a Coulombic efficiency of 91.99% (Table S3, Supporting Information). Therefore, this temperature provides the best balance between micropore insertion and adsorption. Similarly, at a constant temperature of 1000 °C, the changes in structure and performance under different treatment durations were investigated (Figure S17; Tables S4 and S5, Supporting Information). Characterizations verified that hard carbon produced by Joule heating at 1000 °C for 30 s (JH-1000-30) exhibited the most optimized performance among the durations tested. Corresponding comparison samples (TF-1000) were prepared using a tube furnace at the same temperature (1000 °C, 2h) to allow for a comparative analysis of the structural and electrochemical distinctions arising from the different heating methodologies.[22,23]

**Figure 3**a–g presents the HRTEM images of hard carbon materials prepared by tube furnace and rapid Joule heating techniques, along with statistical box plots of their carbon layer length, curvature, and interlayer spacing (Figures S10, S18, and S19, Supporting Information present detailed treatment processes).[24] The HRTEM images show that the samples treated by the tube furnace (Figure 3a,b, Supporting Information) exhibit a distinct ordered layered structure with an interlayer spacing of 0.37 nm. This indicates that the prolonged heating in the tube furnace method facilitates dense stacking of carbon layers. In contrast, the samples prepared by rapid Joule heating (Figure 3c,d) display an interlayer spacing of 0.39 nm, which is characteristic of a looser, more disordered layered structure. The larger interlayer spacing observed in Joule-heated samples, coupled with the rapid heating mechanism, might influence the nature and accessibility of microporosity, including the formation pathways of closed pores that are crucial for sodium storage at low voltages. This altered microstructure is expected to facilitate ion diffusion, and boost electrochemical performance. A further comparison of the selected area electron diffraction (SAED) patterns reveals that both treatment methods show clear amorphous diffraction halos, with the tube furnace-treated samples exhibiting more pronounced diffraction halos, suggesting a higher degree of local graphitic ordering.

The statistical analysis plots (Figure 3e–g) show that TF-1000 and JH-1000-30 samples have similar carbon layer length distribution (Figure 3e). However, in terms of curvature, the TF-1000 samples exhibit lower curvature values, with flatter carbon layers comparing with JH-1000-30 samples with more curved and irregular layer structures (Figure 3f). The box plot of interlayer spacing further confirms than the TF-1000 samples have smaller interlayer spacing (Figure 3g) with a more concentrated distribution comparing with the JH-1000-30 samples. These results suggest that the rapid Joule heating treated samples may have better ion diffusion properties and sodium storage capacity in electrochemical applications due to their larger interlayer spacing, larger carbon layer curvature, and shorter carbon crystallite length.

Furthermore, Raman spectroscopy (Figure 3d) shows that the D band of the JH-1000-30 sample are stronger comparing with the TF-1000 sample, indicating that it has more defects and a lower degree of graphitization. Similarly, in the JH-1000-30 sample, the (002) diffraction peak in the XRD pattern is both broad and of low intensity (Figure 3e). This observation aligns with previous reports[25,26] and indicates the sample's predominantly amorphous structure. The calculated lattice parameters (Figure 3f) further quantified this result. The graphite crystallite size (La, Lc) of the Joule heated sample is smaller and the $I_D/I_G$ ratio is higher, indicating that it has a lower crystallinity and more defects. PDF analysis (Figure 3g) shows that the local structure of the JH-1000-30 sample is more disordered, possibly due to a higher presence of atomic defects, vacancies, or amorphous regions. Additionally, the smaller coordination number (fewer nearest neighbors) indicates that the atomic packing is less dense and more irregular compared to the TF-1000 sample. BET characterization (Figure 3h; Table S6, Supporting Information) shows that its specific surface area is significantly increased, with more micropores and mesopores, which contributed to more efficient sodium storage sites.[27] SAXS (Figure 3i) further verifies that the nanostructure of the Joule heated sample is more complex with more internal pores.[28] X-ray Photoelectron Spectroscopy (XPS) (Figure S20; Table S7, Supporting Information) analysis shows that the Joule heated sample has a slightly higher oxygen content and a larger C-O bond ratio, indicating stronger surface oxidation is higher. And the TF-1000 sample has a higher C=C ratio and a higher degree of graphitization. This is consistent with the Raman and XRD results. In summary, the carbon materials produced by the Joule heating method have a larger specific surface area and more defects, while the tube furnace method can provide a higher degree of graphitization and crystallization.[29]

### 2.3. Electrothermal Coupling Mechanism

The electro-thermal field coupling simulation based on finite element analysis indicates that the local charge accumulation caused by defects (edges/vacancies) in hard carbon significantly alters the electric field distribution (Figure S21, Supporting Information). Current density analysis (**Figure 4**a) reveals a peak charge density of $2.4 \times 10^{13}$ A $m^{-2}$ at the defect core, which is 140% higher than the charge density in the intact lattice region ($1.0 \times 10^{13}$ A $m^{-2}$). This spatial charge modulation, in

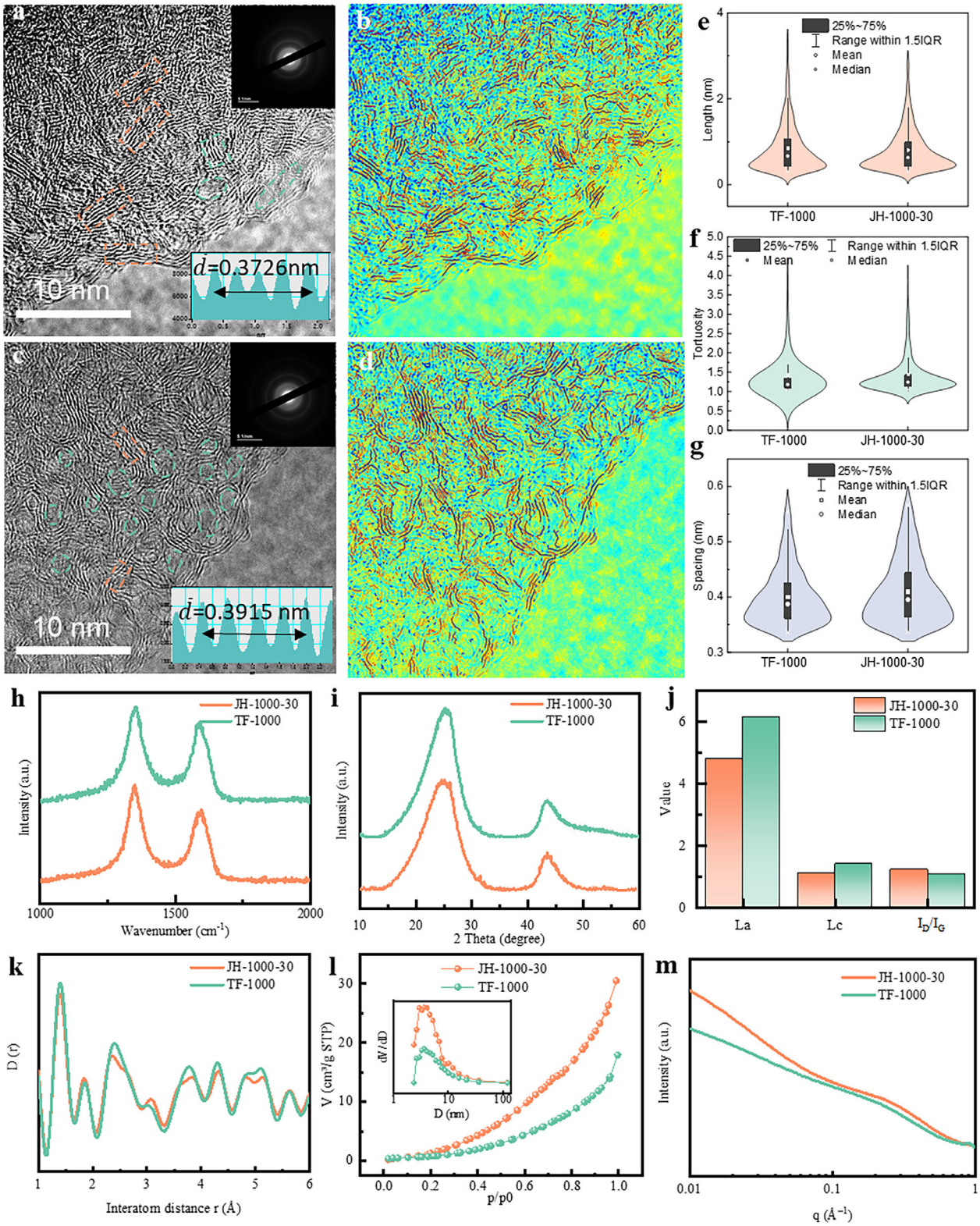


**Figure 3.** Structural characterization of hard carbon materials treated by tube furnace and Joule heating: HRTEM images of hard carbon materials processed by TF-1000 (a-b) and JH-1000-30 (c-d); statistical analysis of carbon layer length (e), curvature (f), and interlayer spacing (g); h) Raman spectra; i) X-ray diffraction (XRD) patterns; j) Statistical analysis of structural parameters, including lateral (La) and vertical (Lc) graphite crystallite sizes and $I_D/I_G$ ratio; k) Pair distribution function (PDF) analysis; l) Brunauer–Emmett–Teller (BET) surface area measurements and pore size distribution; m) Small-angle X-ray scattering (SAXS) patterns.

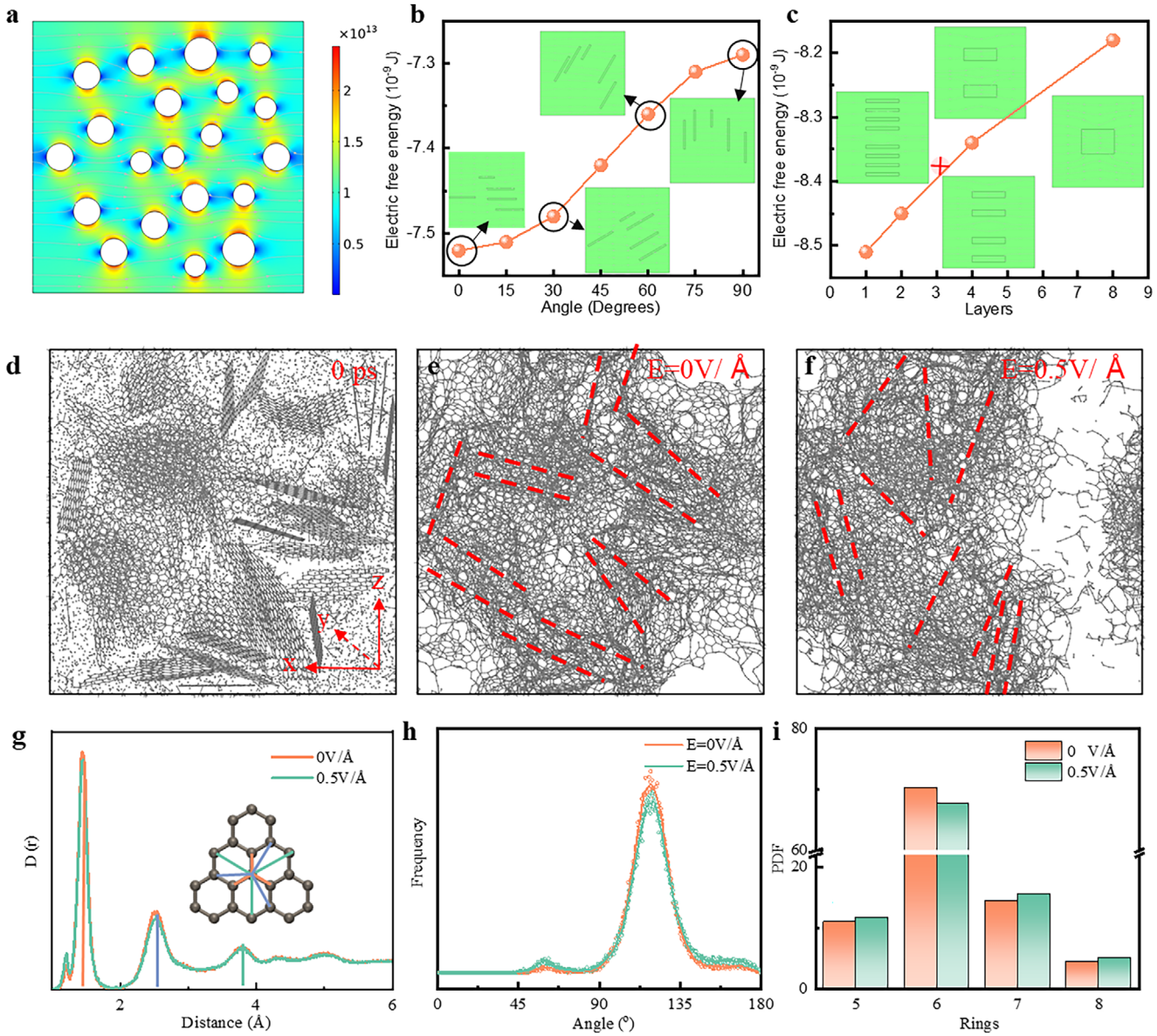


**Figure 4.** Multiscale simulations of electrothermal coupling effects: a) Charge density distribution; b) Free energy evolution during plane alignment; c) Comparison of dispersed (enhanced polarization) vs aggregated graphene sheets; d) ReaxFF MD simulation setup ($80 \times 80 \times 80$ Å$^3$ box, 40 Å visualized thickness); e,f) Temporal evolution of carbon layers without/with electric field (0–80 ps), highlighting edge alignment in E-field (red dashed areas); g) Structural parameter statistics include coordination numbers, h)bond angles, and i) membered rings.

combination with localized Joule heating, can potentially trigger phase transitions or structural reorganization in the material. Additionally, the graphite microcrystals can generate an electric dipole moment response in the electric field, and their deflection follows the principle of free energy minimization. As the angle $\theta$ between the crystal plane and the electric field decreases from 45° (Figure S22, Supporting Information) to 0° (Figure S23, Supporting Information), the system's free energy decreases (Figure 4b), which leads to aligned (002) crystal planes of the microcrystals with the electric field. Notably, dispersed graphite sheets (Figure 4c) are more easily polarized by the electric field due to their high specific surface area, allowing each sheet to independently adjust its orientation to minimize the system free energy. In contrast, aggregated graphite sheets are physically constrained by adjacent layers, and the low-polarization regions formed at the contact interfaces hinder the electric field response, leading to an overall increase in free energy.

ReaxFF molecular dynamics simulations were further employed to verify the evolution of the carbon structure under the influence of an external electric field. The simulation system employed a graphite microcrystal model containing 30,788 atoms (box size: $80 \times 80 \times 80$ Å$^3$), with the thickness of 40 Å (Figure 4d). Analysis of the dynamic trajectory reveals that, in the absence of an electric field (0–80 ps, Figure 4e; Figure S24, Supporting Information), orientation of the carbon layers exhibit dynamic freezing characteristics, with no significant rearrangement and

the randomly arranged configuration. After the application of the electric field (Figure 4f; Figure S25, Supporting Information), the system showed a clear orientation polarization response after 40 ps. By 70–80 ps, the carbon layers in the edge region aligned parallelly to the electric field (highlighted by the red dotted line). This spatiotemporal evolution was positively correlated with the distribution of the electric field.

Statistical analysis of key structural parameters (Figure 4g) confirmed the configurational transformation is driven by the electric field. Compared to the control group, the system subjected to the electric field exhibits a lower carbon-carbon coordination number, a decrease in the proportion of 120° bond angles (Figure 4h), and a reduction in the number of six-membered rings (Figure 4i). These structural changes collectively point to an electric field-induced carbon network reconstruction mechanism, where the external field drives planar distortion and edge reorganization through polarization torque in the $sp^2$ hybridized carbon layers, ultimately forming an amorphous carbon structure with a higher defect concentration.

To investigate the modulation effect of the electric field on the electronic structure, density functional theory (DFT) calculations were performed. As shown in Figure S26 (Supporting Information), with the absence of an external electric field (E = 0 V/Å), the carbon backbone exhibits typical $sp^2$ hybridized delocalized electron characteristics, with a uniform electron density distribution confirming the stability of the chemical bonds. However, after applying an electric field of 0.002 V $Å^{-1}$ (Figure S26b, Supporting Information), the electron density undergoes anisotropic polarization, with a gradient charge redistribution along the electric field direction. This asymmetric polarization induces a differential breaking tendency of the C—C bonds (along the electric field direction) and C—H bonds (against the electric field direction). DFT path analysis (Figure S26c,d, Supporting Information) reveals the dual regulation of the reaction kinetics by the electric field. Under the absence of the electric field, a high energy barrier corresponds to a stable chemical bond structure. After applying a electric field of 0.001 V $Å^{-1}$, the energy barrier sign is reversed, indicating that the electric field lowers the activation energy by electronic redistribution (lowering the electronic energy levels in the reaction zone) and atomic interaction reconstruction (modifying the bonding potential energy surface), thus driving a non-spontaneous reaction.

### 2.4. Electrochemical Performance

The electrochemical performance of JH-1000-30 and TF-1000 was evaluated in Na/C half-cells. The electrochemical performance was analyzed using the Galvanostatic Intermittent Titration Technique (GITT), with a 10-min current pulse at 0.1C followed by a 1-h relaxation period (Figure S27, Supporting Information), revealing distinct sodium ion transport characteristics. Based on the GITT analysis (**Figure 5a**), JH-1000-30 exhibits superior rate capability, evidenced by its consistently lower polarization voltage compared to TF-1000. This enhanced kinetic performance can be attributed to the larger interlayer spacing of the carbon layers for JH-1000-30, which facilitates a faster ion transport rate along with its enriched microporous structure. In addition, the in situ charge-discharge XRD results in Figure S28 (Supporting Information) further verified this conclusion. The (002) peak of JH-1000-30 was significantly broadened during the charge-discharge process, indicating that significantly changed material structure and increased disorder level. Figure S29 (Supporting Information) shows the cyclic voltammograms of JH-1000-30 and TF-1000 electrode materials in the scan rate range of 0.1–1 mV $s^{-1}$. Based on the analysis of the peak current versus the logarithm of scan rate according to the Randles-Sevcik equation,[30] the b-values of JH-1000-30 (Figure 5b) during oxidation/reduction processes are 0.46 and −0.67, which are significantly higher than the corresponding values of TF-1000 (0.35/-0.53). This difference suggests that the Joule heat treatment increased the electrochemical active surface area of JH-1000-30 by ≈31%. Further logarithmic coordinate analysis (Figure S29c,d, Supporting Information) reveals that the b-values of JH-1000-30 for the anodic (0.38) and cathodic (0.29) are higher than those of TF-1000 (0.30/0.24), respectively, whereas the b-values for re below 0.5 indicates that the sodium storage behavior is primarily controlled by solid-state diffusion processes.

To better understand the kinetic difference between TF-1000 and JH-1000-30 during the phase transitions at different stages, we employed in situ electrochemical impedance spectroscopy (EIS). Figure S30 (Supporting Information) displays the Nyquist plots captured during the discharge process. These plots typically feature two incomplete semicircles, representing the solid electrolyte interphase (SEI) layer. The combination of these structural advantages results in a 35.7% reduction in the charge transfer resistance of JH-1000-30 (157 Ω) compared to TF-1000 (101 Ω) (Figure S30, Supporting Information), which is directly related to its superior rate capability (Figure S31, Supporting Information). To further investigate the kinetic changes during the phase transitions of TF-1000 and JH-1000-30 at different stages, we employed in situ electrochemical impedance spectroscopy (EIS). Figure S31 (Supporting Information) shows the Nyquist plots captured during the discharge process, which typically feature two incomplete semicircles corresponding to the solid electrolyte interphase (SEI) layer. To better understand the sub-steps of the electrode process, we applied the Distribution of Relaxation Times (DRT) technique[31–33] (Figure 5c; Figure S32, Supporting Information). The relatively high $\tau 5$ value (Tables S8 and S9, Supporting Information) indicates a slowdown in the charge transfer process. Consequently, the $\tau 4$ and $\tau 5$ steps are considered as rate-determining steps in the sodiation process. The observed reduction in $\tau 4$ and $\tau 5$ resistances for JH-1000-30 further suggests that the Joule-heated sample exhibits faster sodium ion insertion kinetics, particularly during these critical rate-determining steps.

Figure 5d illustrates the typical charge-discharge curves of the TF-1000 and JH-1000-30 samples in sodium-ion batteries. Throughout the entire voltage range, the JH-1000-30 sample exhibits a higher specific capacity. Inset of Figure 5d compares the capacity contributions of the Joule-heated and tube furnace samples at voltages above and below 0.1V, respectively. The Coulombic efficiency of the Joule-heated sample is 92.0%, with a significantly larger capacity contribution of 210.4 mAh $g^{-1}$ in the low voltage range (<0.1V). In contrast, the tube furnace sample has a Coulombic efficiency of 90.9%, with a lower capacity contribution of 171.4 mAh $g^{-1}$ in the same low voltage range. This indicates that the Joule-heated sample demonstrates superior sodium-ion storage capacity at low voltages, due to enriched

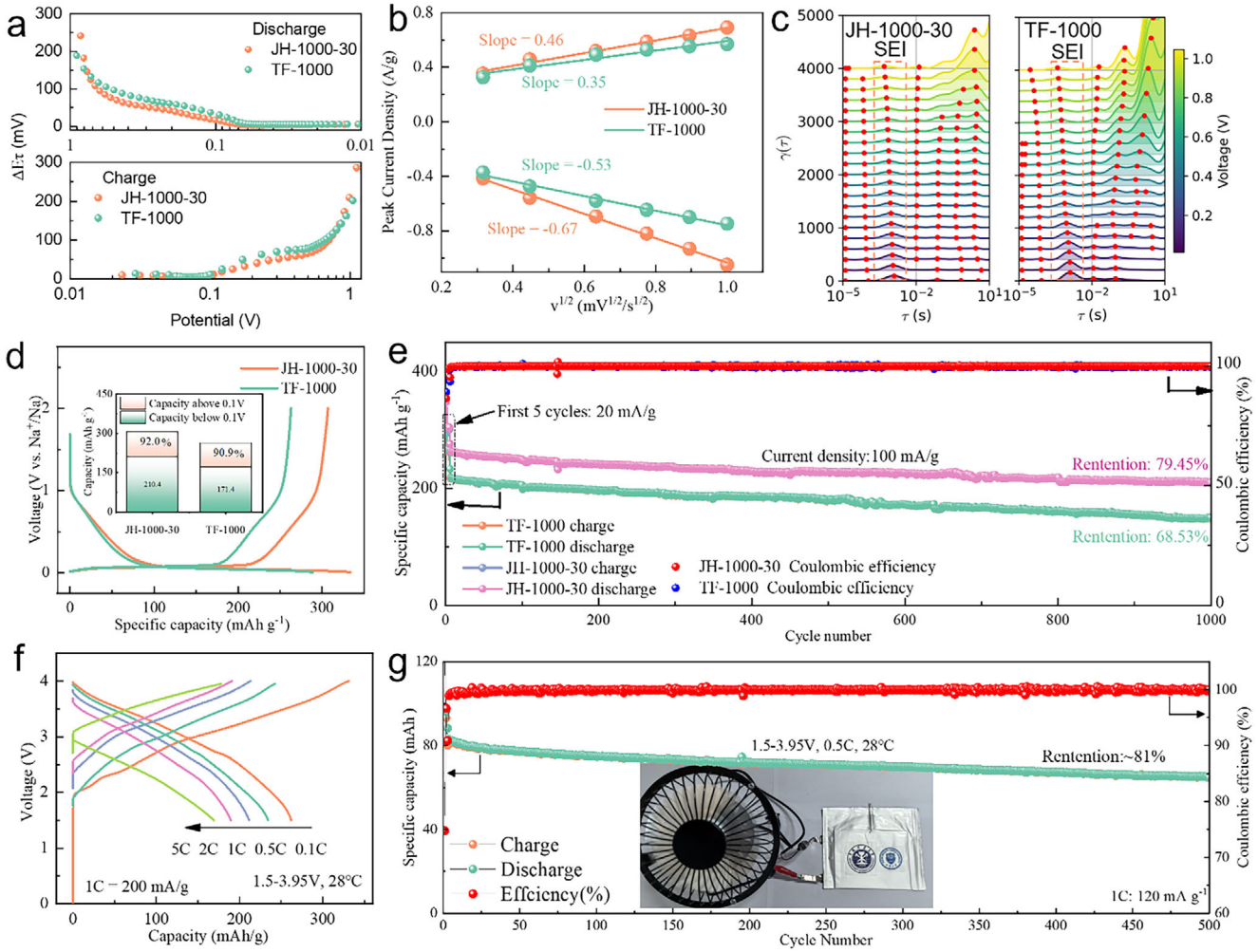


**Figure 5.** Sodium ion diffusion kinetics and electrochemical performance: a) Polarization voltages ($\Delta E\tau$) versus potential during the sodiation process (top-plot) and desodiation process (bottom-plot), derived from GITT measurements; b) Determination of the *b*-value using the relationship between the peak current and the sweep rate; c) DRT analyses of The TB-1000 and JH-1000-30; d) First cycle charge-discharge curves of TB-1000 and JH-1000-30 at a current density of 20 mA $g^{-1}$; e) Cycling performance of TF-1000 and JH-1000-30; f) Charge–discharge profile at 0.1C, 0.5C, 1C, 2C and 5C of the pouch cell; g) Cycling performance of JH-1000-30@NiFeMn333 at a current rate of 0.5C.

microporous structure, corresponding facilitated ion transport and storage. Additionally, the JH-1000-30 exhibits better rate performance than TF-1000 (Figure S31, Supporting Information). After high-rate discharge at 2000 mA $g^{-1}$, capacity of the Joule-heated sample can recover to its initial level when the current density is returned to 20 mA $g^{-1}$, showing excellent structural stability. Figure 5e presents the long-cycle stability of both samples; after 1000 cycles at a current density of 100 mA $g^{-1}$, the capacity retention of JH-1000-30 is 79.45%, while TF-1000 only retains 68.53%. After 1000 cycles, a uniform SEI film of ≈10.58 nm in thickness forms on the electrode surface (Figure S34b, Supporting Information). The complete coverage of the SEI film effectively reduces interfacial impedance and suppresses continuous electrolyte decomposition. Although surface wrinkling occurs (Figure S34c, Supporting Information), no particle cracking is observed, confirming that the material can withstand the volumetric strain caused by the repeated insertion/extraction of sodium ions. EDS mapping (Figure S34d; Table S10, Supporting Information) shows a uniform distribution of C, O, F, and Na elements, with the NaF component forming a dense passivation layer that cooperatively enhances interfacial stability.

To assess the practical viability of JH-1000-30, pouch-type full cells were assembled using an O3-type $NaNi_1/_3Fe_1/_3Mn_1/_3O_2$ layered cathode (NiFeMn333) paired with the JH-1000-30 anode. As shown in Figure 5f, the full cell exhibits stable electrochemical performance under varying cycling conditions (normalized to anode active mass). Long-term cycling at 0.5C (Figure 5g) demonstrates 81% capacity retention after 500 cycles, with a minimal capacity fade rate of 0.038% per cycle. The near 100% coulombic efficiency throughout cycling confirms efficient charge transfer and suppressed parasitic reactions, attributable to the structural compatibility between the JH-1000-30 anode and NiFeMn cathode. A practical demonstration (inset, Figure 5g) shows the cell can successfully power a miniature fan, highlighting its energy density (>130 Wh $kg^{-1}$, Table S11, Supporting Information) sufficient for low-power electronics. These results collectively

underscore the application potential of JH-1000-30 for consumer electronics applications requiring balanced energy output and cycling durability.

## 3. Conclusion

In summary, this study uncovers the mechanism behind the spatiotemporal evolution during the synthesis of hard carbon materials through electrothermal coupling. By precisely controlling the spatial distribution of current density gradients and the time-dependent evolution of Joule heating, we demonstrate how dynamic spatiotemporal effects can reconstruct the microstructure of hard carbon materials. This innovative approach reduces the carbonization time by a factor of 1/240, from 2 h to just 30 s, compared to conventional methods. In situ PDF characterization reveals that Joule heating induces rapid graphitization and the formation of a hierarchical microporous network within 30 s. Electrochemical analysis shows that the optimized JH-1000-30 sample exhibits significantly lower polarization and reduced charge transfer resistance, illustrating the role of electrothermal field gradients in regulating ion migration paths and boosting reaction kinetics. Multi-scale simulations further reveal the spatiotemporal synergistic mechanism of electrothermal coupling: 1) In the spatial dimension, current density gradients create localized Joule heating, leading to the in situ formation of microporous structures via thermodynamic nonequilibrium states; 2) In the temporal dimension, the electric field accelerates the growth of carbon microcrystals and promotes the directional assembly of $sp^2$ carbon domains. These effects result in a first-cycle Coulombic efficiency of 92.0% and a capacity retention of 79.45% after 1000 cycles. By establishing a structure-performance relationship that links electrothermal parameters, spatiotemporal evolution, and performance, this study introduces a novel paradigm for the precise control of hard carbon material synthesis, advancing the design of sodium-ion batteries into a new era of spatiotemporal engineering.

## 4. Experimental Section

*Preparation of Materials*: First, coconut shells were crushed and sieved to particles below 200 mesh to facilitate the subsequent reaction. The crushed shells were then thoroughly washed to remove impurities and ash, followed by drying in an oven at 105 °C for 12 h to eliminate moisture. The dried shells were then pre-carbonized in a tube furnace under a nitrogen atmosphere to prevent oxidation. The temperature was raised to 600 °C at a rate of 5 °C $min^{-1}$ and held constant for 2 h to ensure thorough pre-carbonization. This pre-carbonization step is crucial as it removes the majority of volatile components and significantly enhances the electrical conductivity of the precursor, thereby ensuring more uniform heating in the subsequent Joule heating stage. Furthermore, this pre-carbonization step at ≈600 °C aligns with common industrial practices for biomass precursors like coconut shells. In many regions where these shells are sourced, a preliminary on-site charring process is often employed to reduce volume and moisture content for more economical transportation and handling. After cooling, the pre-carbonized coconut shell material was obtained. Next, the pre-carbonized coconut shell carbon was further processed using an in situ Joule heating carbonization device (Shenzhen Zhongkejingyan Company). This method involved applying electric current directly to heat the material rapidly. To ensure uniform heating and precise temperature control during this ultrafast process, the device employs a real-time current adjustment strategy, which compensates for any dynamic changes in the material's conductivity and maintains the sample at the set temperature. 100 mg of the pre-carbonized coconut shell carbon sample was treated at temperatures of 900, 1000, 1100, 1200, and 1300 °C for 30 s at each temperature. Additionally, for optimization, Joule heating treatments were conducted on pre-carbonized coconut shell carbon sample at different times (0s, 15s, 30s, and 1 min) to investigate the impact of time on material properties. For comparison, traditional tube furnace carbonization was applied to the pre-carbonized coconut shell carbon at 1000 °C, with a heating rate of 5 °C $min^{-1}$ and holding for 2 h under nitrogen. The resulting sample was named TF-1000.

*Material Characterization*: Through synchrotron radiation-based pair distribution function experiments were performed at the beamline BL13SSW at Shanghai Synchrotron Radiation Facility. using synchrotron radiation with an energy of 60.2 keV ($\lambda$ = 0.2061 Å). The *in suit* PDF patterns were recorded every 2s. The collected 2D diffraction patterns were calibrated with standard CeO2 sample by Fit2D software. The morphology and microstructure of sample were studied by SEM (JSM-7800F) and a transmission electron microscope (JEM F200). X-ray powder diffraction (XRD) was conducted using a Bruker D-8 Advance diffractometer with nickel-filtered Cu-K$\alpha$ ($\lambda$ = 1.54178 Å) radiation at room temperature, and the data was collected from 5 to 80° with a scan rate of 2° $min^{-1}$ to obtain the phase structure of sample. Raman measurements were done for the composite by a Raman spectrometer (Senterra, Bruker, Germany) equipped with a 532 nm laser line to determine the chemical composition and structure of sample. X-ray photoelectron spectroscopy (XPS) spectra were collected using a Thermal Scientific ESCALAB 250.

*Electrochemical Characterization*: To prepare the hard carbon anode, the hard carbon material was mixed with sodium alginate (SA) as a binder at a 95:5 mass ratio. The mixture was then combined with deionized water to form a uniform slurry, which was stirred for 6 h at room temperature. The slurry was coated evenly onto copper foil using a coating machine to ensure consistent thickness, which is crucial for uniform electrode performance. The coated electrode was dried in a vacuum oven at 100 °C for 12 h to remove moisture and solidify the active material. After drying, the electrode was cut into 9 mm diameter discs, with a loading of 1.5–2 mg $cm^{-2}$ to ensure repeatability and comparability in electrochemical testing. During battery assembly, all steps were performed in a glove box filled with high-purity argon to prevent contamination by air and moisture. The prepared hard carbon anode was placed in a CR2032 coin cell as the working electrode, with a pre-soaked glass fiber separator (Whatman, GF/F) placed on top. The electrolyte was made by dissolving 1 mol $L^{-1}$ $NaPF_6$ in a 1:1 mixture of ethylene carbonate (EC) and diethyl carbonate (DEC), which shows good conductivity and stability for sodium-ion batteries. A sodium foil counter electrode was placed on top of the separator. The electrolyte was added to ensure proper wetting, and the cell was sealed immediately to maintain airtightness. Electrochemical performance was tested at 25 °C. First, charge-discharge cycling was performed using a NEWARE battery tester, with an appropriate voltage range (0.01–2.00 V) and various current densities. The battery's capacity, cycle stability, and rate capability were evaluated from the charge-discharge curves. Further electrochemical characterization was done using cyclic voltammetry (CV) and electrochemical impedance spectroscopy (EIS) with a CHI660E instrument. CV was performed with a voltage window of 0.01–2.00 V and scan rates from 0.1 to 1.0 mV $s^{-1}$ to study the electrochemical kinetics, while EIS was used to analyze interface and charge transfer resistances, with a frequency range of 100 kHz to 0.01 Hz. sodium -ion storage performance and Galvanostatic Intermittent Titration Technique (GITT) tests were recorded using a Newway battery testing system, with a voltage range of 0.01—2.00 V vs Na+/Na.

*Multiscale Simulation*: COMSOL Multiphysics software was used for finite element analysis to simulate the heat conduction and boundary radiation effects during sample heating. The heat transfer module was used to simulate the heat conduction process under different heating conditions, focusing on the analysis of the heat conduction inside the sample and the radiation heating of the sample boundary by external heat sources. By setting different heating times, the sample temperature changes over time, and the temperature distribution and gradient are analyzed. In addition, COMSOL is also used to simulate the Joule heating process. Joule

heat generates heat through the flow of current, and the "electromagnetic field module" is used to simulate the current distribution and thermal effects. By setting parameters such as current intensity and conductor resistance, the heat caused by the current and its transfer process inside the sample are analyzed. The "heat transfer module" is combined to simulate the diffusion of heat, and the finite element method (FEM) is used to analyze the electric field enhancement and local heating phenomena. At the same time, the "electric field module" is used to simulate the electric field distribution when the current passes through the sample, focusing on the local enhancement effect of defect sites (such as edges, vacancies or impurities), and the "electrostatic module" is used to analyze the polarization effect and free energy change of the graphite sheet in the electric field. Molecular dynamics simulations were performed using LAMMPS, coupled with the ReaxFF reaction force field, to model the dynamic behavior of the carbon layer under an electric field. The ReaxFF force field is capable of simulating chemical reactions and tracking bond formation and breaking, making it ideal for carbon material systems with complex chemical behaviors. The simulation model consists of 30,788 atoms, half of which are graphite microchips and the other half carbon atoms, within a simulation box of 80×80×80 Å. The Poreblazer program[34] was used to analyze the accessible surface area, pore size distribution, structural density, and other pore characteristics after the simulation. Developed by Professor Lev Sarkisov, Poreblazer is a computational tool for characterizing the pore structure of porous materials.

## Supporting Information

Supporting Information is available from the Wiley Online Library or from the author.

## Acknowledgements

This work was supported by the National Natural Science Foundation of China (Nos. 92372107, 52171219, 22109091, 52403307, U21A20325). The authors thank the staff of beamline BL13SSW at Shanghai Synchrotron Radiation Facility for experimental supports.

## Conflict of Interest

The authors declare no conflict of interest.

## Author Contributions

Y.C. and R.T. conceived the concept and designed the experiments. P.H. fabricated the samples, performed electrochemical measurements, and analyzed the data. P.H. wrote the manuscript, and all authors contributed to the discussion and provided feedback on the manuscript.

## Data Availability Statement

The data that support the findings of this study are available from the corresponding author upon reasonable request.

## Keywords

electrothermal coupling, hard carbon, sodium-ion batteries, spatiotemporal evolution, ultrafast joule heating

Received: April 21, 2025
Revised: June 24, 2025
Published online:

[1] Y. Li, A. Vasileiadis, Q. Zhou, Y. Lu, Q. Meng, Y. Li, P. Ombrini, J. Zhao, Z. Chen, Y. Niu, X. Qi, F. Xie, R. van der Jagt, S. Ganapathy, M.-M. Titirici, H. Li, L. Chen, M. Wagemaker, Y.-S. Hu, *Nat. Energy* **2024**, *9*, 134.
[2] F. Zhang, B. He, Y. Xin, T. Zhu, Y. Zhang, S. Wang, W. Li, Y. Yang, H. Tian, *Chem. Rev.* **2024**, *124*, 4778.
[3] D. Dewar, A. M. Glushenkov, *Energy Environm. Sci.* **2021**, *14*, 1380.
[4] P. Huang, Z. Miao, Z. Li, L. Chen, Y. Li, Z. Liu, J. Zhang, J. Luo, W. Zhang, W.-D. Liu, X. Zhang, R. Zhu, Y. Chen, *Prog. Nat. Sci.: Mater. Int.* **2024**, *34*, 1207.
[5] N. Lege, X.-X. He, Y.-X. Wang, Y. Lei, Y.-X. Yang, J.-T. Xu, M. Liu, X. Wu, W.-H. Lai, S.-L. Chou, *Energy Environm. Sci.* **2023**, *16*, 5688.
[6] J. C. Hyun, H. M. Jin, J. H. Kwak, S. Ha, D. H. Kang, H. S. Kim, S. Kim, M. Park, C. Y. Kim, J. Yoon, J. S. Park, J.-Y. Kim, H.-D. Lim, S. Y. Cho, H.-J. Jin, Y. S. Yun, *Energy Environ. Sci.* **2024**, *17*, 2856.
[7] Y. Zeng, J. Yang, H. Yang, Y. Yang, J. Zhao, *ACS Energy Lett.* **2024**, *9*, 1184.
[8] M. A. Reddy, M. Helen, A. Gross, M. Fichtner, H. Euchner, *ACS Energy Lett.* **2018**, *3*, 2851.
[9] C. Yu, Y. Li, H. Ren, J. Qian, S. Wang, X. Feng, M. Liu, Y. Bai, C. Wu, *Carbon Energy* **2023**, *5*, 220.
[10] S. Ma, W. Yan, Y. Dong, Y. Su, L. Ma, Y. Li, Y. Fang, B. Wang, S. Wu, C. Liu, S. Chen, L. Chen, Q. Huang, J. Wang, N. Li, F. Wu, *Mater. Today* **2024**, *75*, 334.
[11] Z. Guo, H. Jiang, X. Sun, X. Li, Z. Liu, J. Zhang, J. Luo, J. Zhang, X. Tao, J. Ding, X. Han, R. Liu, Y. Chen, W. Hu, *Adv. Energy Mater.* **2024**, *14*, 2302484.
[12] J. Luo, J. Zhang, Z. Guo, Z. Liu, C. Wang, H. Jiang, J. Zhang, L. Fan, H. Zhu, Y. Xu, R. Liu, J. Ding, Y. Chen, W. Hu, *Adv. Mater.* **2024**, *36*, 2405956.
[13] S. Dou, J. Xu, D. Zhang, W. Liu, C. Zeng, J. Zhang, Z. Liu, H. Wang, Y. Liu, Y. Wang, Y. He, W. Liu, W. Gan, Y. Chen, Q. Yuan, *Angew. Chem. Int. Ed.* **2023**, *62*, 202303600.
[14] S. Liu, Y. Shen, Y. Zhang, B. Cui, S. Xi, J. Zhang, L. Xu, S. Zhu, Y. Chen, Y. Deng, W. Hu, *Adv. Mater.* **2022**, *34*, 2106973.
[15] S. Dou, Y. Shao, L. Fan, D. Zhang, J. Xu, J. Zhang, H. Tian, Y. He, C. Mao, H. Zhu, W. Gan, J. Zeng, W. Liu, J. Zhou, Y. Chen, Q. Yuan, *Adv. Funct. Mater.* **2025**, *35*, 2412551.
[16] P. Huang, R. Zhu, X. Zhang, W. Zhang, *Chem. Eng. J.* **2022**, *450*, 137999.
[17] L. Eddy, S. Xu, C. Liu, P. Scotland, W. Chen, J. L. Beckham, B. Damasceno, C. H. Choi, K. Silva, A. Lathem, Y. Han, B. I. Yakobson, X. Zhang, Y. Zhao, J. M. Tour, *J. Am. Chem. Soc.* **2024**, *146*, 16010.
[18] J. Wang, J.-H. Park, A.-Y. Lu, J. Kong, *J. Am. Chem. Soc.* **2022**, *144*, 22925.
[19] Z. Li, P. Huang, J. Zhang, Z. Guo, Z. Liu, L. Chen, J. Zhang, J. Luo, X. Tao, Z. Miao, H. Jiang, C. Wang, X. Ye, X. Wu, W.-D. Liu, R. Liu, Y. Chen, W. Hu, *Energy Environ. Sci.* **2025**, *18*, 2962.
[20] Y. Chen, S. Xu, S. Zhu, R. J. Jacob, G. Pastel, Y. Wang, Y. Li, J. Dai, F. Chen, H. Xie, B. Liu, Y. Yao, L. G. Salamanca-Riba, M. R. Zachariah, T. Li, L. Hu, *Nano Res.* **2019**, *12*, 2259.
[21] H. Kim, J. C. Hyun, D.-H. Kim, J. H. Kwak, J. B. Lee, J. H. Moon, J. Choi, H.-D. Lim, S. J. Yang, H. M. Jin, D. J. Ahn, K. Kang, H.-J. Jin, H.-K. Lim, Y. S. Yun, *Adv. Mater.* **2023**, *35*, 2209128.
[22] N. Sun, Z. Guan, Y. Liu, Y. Cao, Q. Zhu, H. Liu, Z. Wang, P. Zhang, B. Xu, *Adv. Energy Mater.* **2019**, *9*, 1901351.
[23] G. Ryoo, J. Shin, B. Guk Kim, D. Geun Lee, J. Tark Han, B. Park, Y. Oh, S. Yol Jeong, S.-H. Lee, D. Yun Lee, D. Kim, J. Hwan Park, *Chem. Eng. J.* **2024**, *496*, 154081.
[24] J. Li, H. Ouyang, J. Wang, J. Li, H. Zhang, *J. Electrochem. Soc.* **2022**, *169*, 090522.

[25] Y. Cui, C. M. Subramaniyam, L. Li, T. Han, M.-A. Kang, J. Li, L. Zhao, X. Wei, A. J. Svagan, M. M. Hamedi, *J. Mater. Chem. A* **2022**, *10*, 9059.
[26] X. Zhao, C. Yang, X. Gan, L. Gong, X. Yan, I. Zhitomirsky, K. Shi, *Energy Fuels* **2022**, *36*, 13408.
[27] D. Cheng, X. Zhou, H. Hu, Z. Li, J. Chen, L. Miao, X. Ye, H. Zhang, *Carbon* **2021**, *182*, 758.
[28] J. Wang, L. Yan, B. Liu, Q. Ren, L. Fan, Z. Shi, Q. Zhang, *Chin. Chem. Lett.* **2023**, *34*, 107526.
[29] J. Li, Z. Li, S. Tang, J. Hao, T. Wang, C. Wang, L. Pan, *Carbon* **2023**, *203*, 469.
[30] Z. Abdi, M. Vandichel, A. S. Sologubenko, M.-G. Willinger, J.-R. Shen, S. I. Allakhverdiev, M. M. Najafpour, *Int. J. Hydrogen Energy* **2021**, *46*, 37774.
[31] A. Weiß, S. Schindler, S. Galbiati, M. A. Danzer, R. Zeis, *Electrochim. Acta* **2017**, *230*, 391.
[32] T. H. Wan, M. Saccoccio, C. Chen, F. Ciucci, *Electrochim. Acta* **2015**, *184*, 483.
[33] Y. Lu, C.-Z. Zhao, J.-Q. Huang, Q. Zhang, *Joule* **2022**, *6*, 1172.
[34] L. Sarkisov, A. Harrison, *Mol. Simul.* **2011**, *37*, 1248.